





HR-Si prism coupled tightly confined spoof surface plasmon polaritons mode for terahertz sensing

YI HUANG,¹ SHUNCONG ZHONG,^{1,2,*}  TINGTING SHI,¹ YAO-CHUN SHEN,³  AND DAXIANG CUI⁴

¹Laboratory of Optics, Terahertz and Non-Destructive Testing, School of Mechanical Engineering and Automation, Fuzhou University, Fuzhou 350108, China

²Department of Precision Mechanical Engineering, School of Mechatronic Engineering and Automation, Shanghai University, 200072, China

³Department of Electrical Engineering and Electronics, University of Liverpool, L69 3BX, UK

⁴Department of Bio-Nano Science and Engineering, Shanghai Jiaotong University, 200030, China

*zhongshuncong@hotmail.com

Abstract: We report a high-resistivity silicon (HR-Si) prism coupled terahertz (THz) spoof surface plasmon polaritons (SSPPs) on flat subwavelength metasurface. Using a high refractive index prism as an external coupler, a more tightly confined SSPPs mode can be excited in a smaller resonant cavity, leading to strong light-matter interaction. Besides, theoretical analysis and experimental results have both indicated that the SSPPs resonance response to the filling patterns of analyte in the resonant cavity are quite different. In particular, we have found that the interaction between analyte and SSPPs wave can be maximized when the analyte filled with the whole resonant cavity and a higher sensitivity for THz sensing can be obtained. A high sensitivity varied from 0.31 THz/RIU to 0.85 THz/RIU is predicted. Furthermore, these SSPPs modes exhibit high Q-factor, and characteristic spectra of water caused by surface plasmon resonance (SPR) are observed, which is significant in promoting the THz-SPR sensing of polar liquids or aqueous analytes with THz metasurfaces.

© 2019 Optical Society of America under the terms of the [OSA Open Access Publishing Agreement](#)

1. Introduction

Terahertz (THz) radiation, between microwave and infrared (0.1 THz-10 THz), is known as “terahertz gap” [1,2]. Over the past 20 years, THz technology is developed unprecedentedly with the development of ultrafast laser, which has attractive advantages and broad prospects in biology, chemistry, physics, and astronomy [3–6]. THz technology is considered highly appealing for sensing applications, particularly in biosensing [7] and security [8] due to the peculiar properties of absolutely non-ionizing and broadband molecular “fingerprint” spectra of THz radiation [9,10]. However, the broad use of THz technology in THz sensing is greatly impeded by the scarcity of high average power THz source that resulting in weak interactions between it and analytes [11].

Fortunately, THz metasurfaces has attracted considerable attentions and became a hot study field in THz sensing for its ability to generate strongly confined electromagnetic field to enhance light-matter interactions and form sharp spectral features resulted from surface plasmon resonance (SPR) [12]. Consequently, a series of researches have been conducted on THz sensing using planar THz metasurfaces with structured metallic surfaces, such as slant crosses [13], complementary crosses [14], asymmetric split ring [15], U-shaped split ring [7], C-shaped split ring [16] and subwavelength grooves [17,18], and gain a lot of valuable research results. However, when it comes to sensing polar liquids or aqueous analytes, the energy of THz electromagnetic field is weakened severely owing to strong absorption in transmission mode [19]. Thus, the transmission measurements of metasurfaces are often limited to the detection of minute quantities of analytes

with lower losses. That is the main limitation for the widespread application of THz-SPR technology in sensing, especially in biosensing near physiological conditions containing aqueous solutions. Although THz spectroscopy combines the surface plasmon resonance (SPR) technology exhibits ultrahigh sensitivity to small changes in the dielectric environment [20,21], its sensitivity can be drastically reduced in the case that analyte is placed outside the main resonance cavity where severe field intensity attenuation occurs [22]. Thus, the excitation of tightly confined spoof surface plasmon polaritons (SSPPs) [23] modes with improved spatial overlap with the analyte has become the key point of research.

In this work, a high resistivity silicon (HR-Si) prism coupled terahertz metasurface sensor is proposed and experimentally demonstrated. Firstly, the dielectric response of silicon wafers with different resistivity were investigated by transmission measurement with THz time-domain spectroscopy (THz-TDS). The high transmissibility and refractive index of HR-Si material in THz regime make it become a leading option for the fabrication of the key component of an attenuated total reflection (ATR) [24] setup, i.e., THz prism. Compared to low refractive index prism, a more tightly confined SSPPs mode can be excited in a smaller resonant cavity resulting in strong light-matter interaction as larger wavevector can be matched with high refractive index HR-Si prism. Secondly, a deep study of the SSPPs resonance response to the filling patterns of analyte in the resonant cavity between coupling gap and grooves was conducted through experiments and dispersion curves analysis. A significant improvement of the sensitivity is obtained because the interaction between analyte and SSPPs wave can be maximized when the analyte filled with the whole resonant cavity. Meanwhile, our experimental results also show that the strong absorption of terahertz radiation by water can be alleviate effectively and sharp spectral features of water caused by the SPR are observed from the obtained THz spectra that cannot be accessed directly by common transmission technique [25,26]. The proposed THz metasurface integrated HR-Si prism device provide the possibility for developing more reliable detection of polar liquids or aqueous solutions.

2. Device design and physical mechanism

The schematic diagram of the SSPPs excitation on subwavelength metasurface with the HR-Si prism based Otto configuration [27] is shown in Fig. 1(a). Our metallic metasurface consists of one-dimensional (1D) array of subwavelength trapezoidal grooves with operating frequency range between 0.2 and 1 THz. The trapezoidal grooves decorated metallic metasurface is fabricated via a multistep process. Firstly, a thickness of approximately 2 μm of AZ 5214E positive photoresist layer was coated onto a 500 μm thick silicon wafer via spin coating process (spun at 2000 rpm for 30 s followed by a soft bake at 100 $^{\circ}\text{C}$ for 60 s). Secondly, the photoresist is exposed to UV light via a pre-fabricated photomask in a mask aligner (Karl Suss, MA6/BA6) and developed with AZ 400K developer to reveal the etched mask of groove array. After that, the trapezoidal groove array (with a varying groove width with the depth of the grooves), with an overall area of 20 mm \times 35 mm, was patterned on the Si substrate via conventional deep reactive ion etching (DRIE) using Bosch process with a chamber pressure of 10 mTorr, an radio frequency of 13.56 MHz, and a gas flow rate of 450 sccm. Finally, a 600 nm thick layer of gold is sputtered onto the corrugated silicon wafer to give the final metallic metasurface. Due to the gold film is much thicker than its skin depth in THz regime (approximately 80 nm at 1 THz), the fabricated metasurface closely resembles a decorated perfect electrical conductor surface. The gold film and structured Si substrate are depicted as the yellow and gray regions in Fig. 1(a), respectively. The unit cell of the final trapezoidal groove array has a period of $p = 60 \mu\text{m}$, top width of $w_t = 31 \mu\text{m}$, bottom width of $w_b = 21 \mu\text{m}$, and depth of $h = 90 \mu\text{m}$ (which measured by a film-thickness meter because of their larger depths), as shown in Fig. 1(b). Compared with the reported 2D metamaterials [13–16,28–30], this corrugated metallic structure supports highly confined TM-polarized SSPPs modes which is easier to be tailored by properly designing the geometry because of its simple 1D

structure [31,32]. To excite the SSPPs wave, an evanescent wave was created by the total internal reflection of an incident TM-polarized THz wave at the bottom of the HR-Si ($\rho_{\text{Si}} = 10\text{k Ohm}\cdot\text{cm}$) prism. Once the SSPPs wave is excited, their electrical field is confined around the corrugated metallic surface, which exhibits ultrahigh sensitivity to small changes of the analytes that filled in the resonant cavity between the prism base and the metasurface. Finally, the reflected THz wave was detected to record the electromagnetic response of the hybrid structure as depicted in Fig. 1(a).

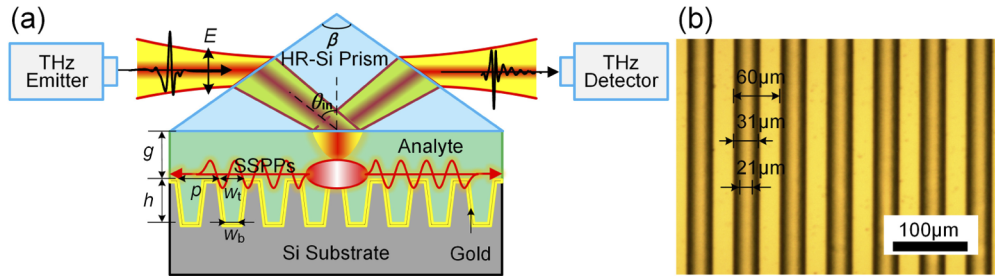


Fig. 1. (a) Exciting SSPPs on subwavelength trapezoidal grooves metasurface with the HR-Si prism based Otto configuration; (b) Optical microscopy image of the fabricated metasurface with a period of $p = 60\ \mu\text{m}$, top width of $w_t = 31\ \mu\text{m}$, bottom width of $w_b = 21\ \mu\text{m}$ and depth of $h = 90\ \mu\text{m}$.

Prior to the processing of HR-Si prism, the transmission measurements of three different resistivity silicon wafers: $\rho_{\text{Si}} < 0.005\ \text{Ohm}\cdot\text{cm}$, $\rho_{\text{Si}} = 2\text{-}4\ \text{Ohm}\cdot\text{cm}$, and $\rho_{\text{Si}} = 10\text{k Ohm}\cdot\text{cm}$, were performed by THz-TDS for the examination of material properties of Si in the THz regime. Note that these experiments were performed in a nitrogen-purged chamber with relative humidity less than 5% to avoid water vapor absorption of terahertz. Repeated measurements made with micrometer give their thicknesses of 0.530 mm, 0.435 mm, and 0.497 mm, respectively. Compared with the reference $E_{\text{ref}}(t)$ (without sample), all of the time-domain waveforms $E_{\text{sam}}(t)$ (Typically, only the first reflected pulse retained and the rest of the waveform is windowed out) are reshaped, attenuated, and time shifted as shown in Fig. 2(a). Remarkably, the terahertz signal is completely attenuated after passed through the silicon wafer with $\rho_{\text{Si}} < 0.005\ \text{Ohm}\cdot\text{cm}$. Furthermore, the electric field of transmitted THz wave increases greatly as ρ_{Si} increases. The time-domain waveform of the silicon wafer with $\rho_{\text{Si}} = 10\text{k Ohm}\cdot\text{cm}$ is similar to the reference $E_{\text{ref}}(t)$, which means that HR-Si has low losses in THz regime. The transmittance of the sample can be calculated using the following formulas:

$$E_{\text{sam}}(\omega)/E_{\text{ref}}(\omega) = Ae^{i\phi}, \quad (1)$$

$$T(\omega) = |A(\omega)|^2, \quad (2)$$

where $E_{\text{sam}}(\omega)$ and $E_{\text{ref}}(\omega)$ denote sample and reference frequency-domain amplitude spectra respectively, which are obtained by fast Fourier transform (FFT). Although part of the energy is reflected [33], the HR-Si maintaining 47-52% transmission from 0.2 THz to 1 THz that significantly higher than the low-resistivity silicon (LR-Si) as shown in the transmission spectra of Fig. 2(a). The dielectric permittivity of materials in THz regime can be calculated using an optical constants model proposed by Dorney [33] and Duvillaret [34] as:

$$n(\omega) = (\phi(\omega)c)/(\omega d) + 1, \quad (3)$$

$$\alpha(\omega) = 2\kappa(\omega)\omega/c = (2/d) \ln[(4n(\omega)) / (A(\omega)(n(\omega) + 1)^2)], \quad (4)$$

$$\varepsilon_1 + i\varepsilon_2 = (n(\omega) + i\kappa(\omega))^2. \quad (5)$$

where d is the thickness of sample, $n(\omega)$ and $\kappa(\omega)$ are the real and imaginary part of refractive index of sample. From the Fig. 2(b), it can be seen that real and imaginary part of dielectric permittivity for both silicon wafers converges to high frequency value of around 11.67 and 0.09, respectively. Moreover, it is obvious that the imaginary part of HR-Si is smaller than that of LR-Si, which further demonstrates that HR-Si has lower loss. The good transmission performance and high dielectric permittivity of HR-Si in THz regime, making them become a good material for the fabrication of THz-ATR prism. Thus, HR-Si was utilized to make the prism with apex angle $\beta = 120^\circ$, internal incident angle $\theta_{in} = 45^\circ$ as shown in Fig. 1(a). The inset of Fig. 2(b) shows the penetration depth of the evanescent wave L_p created by HR-Si prism at prism-air interface, which defined as the decaying length to $1/e$, could be expressed as [31]:

$$L_p = c \left/ \left(\omega \sqrt{(n_p \sin \theta_{in})^2 - (n_d)^2} \right) \right. \quad (6)$$

where $n_p = 3.416$ is the refractive index of HR-Si prism, $n_d = 1$ is the refractive index of air. As it can be seen, the L_p falls with frequency increases, between $110 \mu\text{m}$ and $25 \mu\text{m}$ in our operating frequency (0.2 and 1 THz). We also plot the L_p of polyethylene (PE) prism (with $n_p = 1.54$, $\beta = 120^\circ$, and $\theta_{in} = 64^\circ$) [32] at prism-air interface. As comparison, the HR-Si prism has a shorter L_p due to its larger refractive index. Since the typical length scale of coupling gap (between prism and metasurface) is mainly determined by the compositive effect from the evanescent wave at prism base and the SSPPs wave on the metasurface [31], high refractive index prism may be used to form more confined resonant cavity to enhance light-matter interactions. Because the L_p is much longer than that in visible light, so the coupling gap can be exactly controlled with a high-precision translation stage.

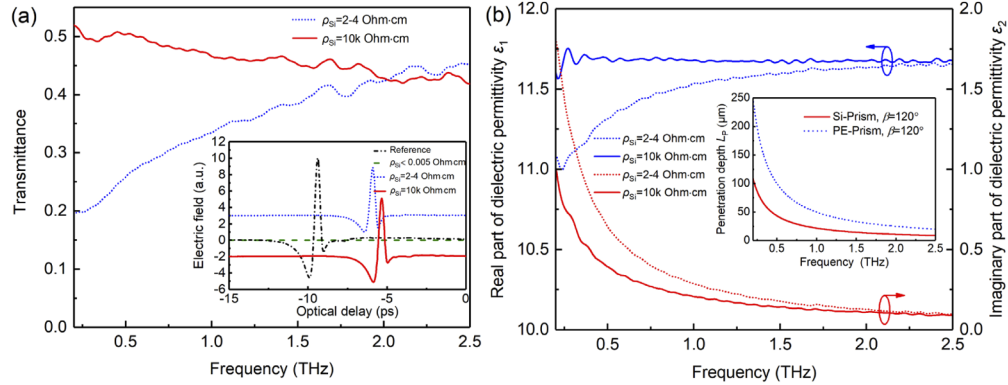


Fig. 2. (a) Experimentally measured transmission spectra of silicon wafers with different resistivity. The inset shows the time-domain waveforms from THz-TDS transmission measurement of silicon wafers with different resistivity ρ_{Si} . (b) Real and imaginary part of dielectric permittivity of silicon wafers (ε_1 and ε_2) with different resistivity. The inset shows the penetration depth of the evanescent wave L_p created by the HR-Si ($\rho_{Si} = 10\text{k Ohm}\cdot\text{cm}$) prism and PE prism at prism-air interface, respectively.

In the limit of width $w_{\text{eff}}, p \ll \lambda$, the dispersion relation of the SSPPs wave on the subwavelength metasurfaces perforated with planar periodic rectangular grooves with w_{eff} , i.e., $w_{\text{eff}} = w_t = w_b$ can be derived by an effective medium approximation model as [35]:

$$k_{\text{SSPPs}} = (\varepsilon_d k_0^2 + ((w_{\text{eff}} \varepsilon_d) / (p \varepsilon_g))^2 k_g^2 \tan^2(k_g h))^{1/2}, \quad (7)$$

where $k_g = k_0 \sqrt{\epsilon_g} (1 + l_s(i+1)/w_{\text{eff}})^{1/2}$ is the wavevector inside in the grooves, $k_0 = 2\pi f/c$ is the vacuum wavevector; ϵ_g and ϵ_d denote the permittivity of the media inside in the grooves and the top semi-infinite space of the metasurface; and $l_s = (k_0 \text{Re} \sqrt{-\epsilon_m})^{-1}$ denote the skin depth of gold, where ϵ_m is the complex permittivity of gold. The solutions for $w_{\text{eff}} = w_b = 21 \mu\text{m}$ (red, dash-dot) and $w_{\text{eff}} = w_t = 31 \mu\text{m}$ (pink, dash) are plotted in Fig. 3. As it can be seen, both SSPPs dispersion curves deviate from the vacuum light and intersect with the lines of the parallel wavevector:

$$k_{\parallel} = n_p(\omega/c) \sin \theta_{\text{in}} = k_{\text{SSPPs}}. \quad (8)$$

(the frequency of the intersection, i.e., the resonance frequency of the SSPPs), which mean that the momentum mismatch between the highly confined plasmon modes and the incident radiation can be overcome via prism. More importantly, larger wavevector can be matched with the high refractive index HR-Si prism. Furthermore, we can find that the dispersion relation calculated by finite element method (FEM) with COMSOL software for our fabricated corrugated metallic metasurface, between two theoretical dispersion relation curves. In particular, for smaller wavevector k , it is closer to the case of $w_{\text{eff}} = 31 \mu\text{m}$ while it approaches gradually to that of $w_{\text{eff}} = 21 \mu\text{m}$ with k increases. The reason is that the trapezoidal shape groove walls of the fabricated metasurface resulting in a varying groove width with the depth of the grooves. The electric field distributions for the unit cell of the trapezoidal grooves at different k , as shown in the insets of Fig. 3. It is obvious that the electric field distribution of the trapezoidal groove permeates gradually from the groove top to the groove inside with k increases when the SPR happens, leading to the change of the electric field distribution. Moreover, the electric field of the SSPPs mode with higher k are more confined to the metasurface. As is mentioned above, the excitation of the more confined SSPPs mode using high refractive index HR-Si prism will further promote the light-matter interaction.

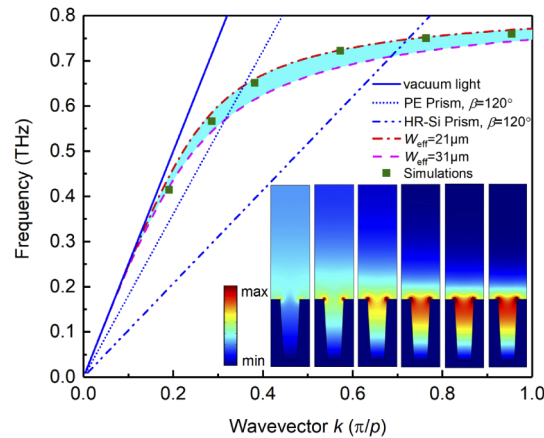


Fig. 3. SSPPs dispersion curves for corrugated metallic metasurfaces in the Brillouin zone. The blue solid line is the vacuum light, and the dotted and double dot-dash line are the parallel wavevector k_{\parallel} for PE and HR-Si prism, respectively. The dot-dash and dash curve shows the effective medium approximation model calculation for rectangular shape grooves, and green points indicate the FEM calculation with COMSOL software for trapezoidal shape grooves. The insets show the electric field distributions for the unit cell of the trapezoidal grooves at different wavevector k .

To explore the impact of the filling patterns of analyte in the resonant cavity on the SSPPs modes, we plotted the SSPPs dispersion curves of the metasurface in two cases: water filled in the grooves (P1), and water filled in the gap and grooves (P2, i.e., the whole resonant cavity). As

seen from Fig. 4, the dispersion curve of the P2 behaves a sharp increase at the region close to the parallel wavevector line of HR-Si prism, and has a lower cutoff frequency than that for the P1. Hence, the shift of the theoretical resonance frequency for P2 has a steeper drop than that for P1 (i.e., $\Delta f_1 < \Delta f_2$), which imply that analytes filled in the gap and grooves can offer a larger sensitivity (defined as the change in resonance frequency per RIU) for THz sensing.

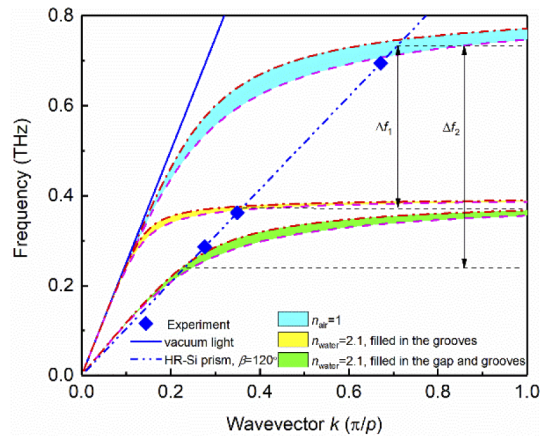


Fig. 4. SSPPs dispersion curves for two different filling patterns of water: filled in the grooves, and filled in the gap and grooves. The scatter data are the experimental results.

Furthermore, we plotted the theoretical resonance frequencies against the refractive index for two different filling patterns of analytes by solving Eqs. (7) and (8), as shown in Fig. 5. By comparison, the theoretical resonance frequency curve of P2 is obviously lower than that of P1. The absolute gradient of the resonance frequency curves (i.e., sensitivity S_n) were also calculated to make it more intuitive, as shown in the inset of Fig. 5. We can clearly see that the sensitivity of P2 varied from 0.31 THz/RIU to 0.85 THz/RIU when refractive index varied from 1 to 2.2, which is significantly higher than that of P1. All these sensitivities are higher than those results reported previously in Refs. [17]. For example, the maximum sensitivities of about 0.13 THz/RIU for

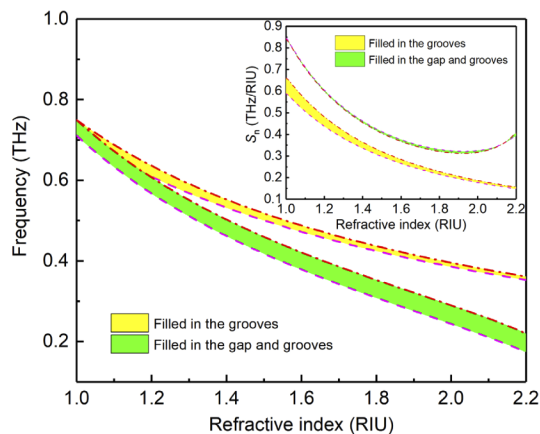


Fig. 5. Theoretical resonance frequency as a function of the refractive index for two different filling patterns of materials. The inset shows the absolute gradient of the resonance frequency curves, i.e., sensitivity S_n .

the V-grooves metasurface and 0.06 THz/RIU for the rectangular grooves metasurface with the direct excitation of SSPPs.

3. Results and discussion

Figure 6 plots the simulated reflectivity spectra by COMSOL software for the two different prisms mentioned above. We can see clearly that the optimal resonance frequency (i.e., reflectivity $R = 0$) shifts from 0.629 THz with $g = 190 \mu\text{m}$ for PE prism to 0.741 THz with $g = 45 \mu\text{m}$ for HR-Si prism, which compare well with the previous theoretical analysis. From the electric field and the time-average energy density distributions for the unit cell of the trapezoidal grooves (as shown in the insets of Fig. 6), we can further see that high refractive index HR-Si prism is significant for the excitation of the tightly confined SSPPs mode. It plays an active part in diminutive resonant cavity formation, which should be very important in THz sensing. Thus, HR-Si prism is utilized as an external surface plasmon coupler to excite the SSPPs.

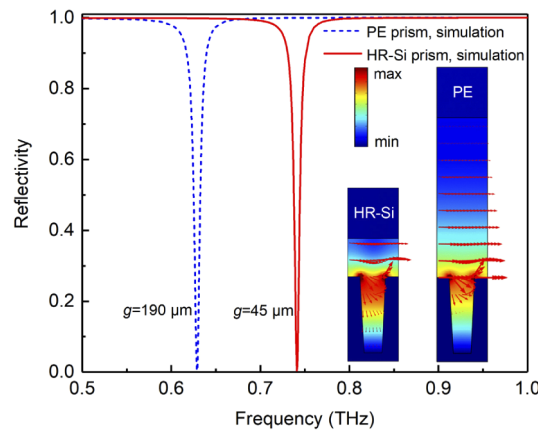


Fig. 6. Simulated reflectivity spectra for two different prisms using COMSOL software. The insets show the electric field and the time-average energy density distributions for the unit cell of the trapezoidal grooves.

The THz time-domain spectroscopy with the HR-Si prism attenuated total reflection (TDS-ATR) was utilized for the SSPPs excitation. Figure 7 shows the experimental time-domain waveforms 7(a), reflected spectra 7(b), and reflectivity spectra 7(c) from the measurement of free-space coupling between THz radiation and SSPPs at different gaps g . Note that the experimental time-domain waveforms are shifted for visual clarity. The reference signals of the time-domain waveforms are obtained when the coupling gap is large enough. Since the observed ATR spectra are similar to that of the transmission type, the reflectivity can be calculated as:

$$R = |E_{\text{sam}}(\omega)/E_{\text{ref}}(\omega)|^2. \quad (9)$$

As it can be seen, the time-domain waveforms modulated by the subwavelength metasurface under SPR condition, which show pronounced ringing that persists for more than 10 ps, and their amplitude of the electric field are reduced slightly. For further observation of the responses of terahertz signal to the changes of coupling gap, the detected time-domain waveforms were converted to the frequency-domain spectra using FFT, as shown in Fig. 7(b). All reflected spectra exhibit distinct dips for different coupling gaps. This is because THz radiation of the dip is coupled into the SSPPs wave which propagates along the metasurface when the momentum matching condition is satisfied. The optimal coupling takes place at the frequency of 0.695 THz

for $g = 45 \mu\text{m}$. Its corresponding reflectivity spectrum (as shown in the Fig. 7(c)) presenting a full width at half maximum (FWHM) of 117 GHz, and a Q-factor (is quality factor for the characterization of the properties of SSPPs resonance, a high Q-factor contributes to the high resolution in spectral characterization, which defined as the ratio of the resonant frequency to the FWHM, i.e., $Q\text{-factor} = f/\text{FWHM}$) of approximately 6, imparting to the proposed sensor the capability of high-performance THz-SPR sensing for the refractive index detection. Remarkably, the shift and expansion of the dip occurs at narrower gaps or where the SSPPs fields are more intense due to the additional damping resulting from the presence of the prism [36]. The ability to adjust the resonance frequency of SSPPs by properly controlling the coupling gap, which means that such THz metasurface device with the Otto geometry might be a very flexible platform for an enhanced detection of molecular THz absorption spectra. This is because the enhancement of the electric field associated with the SPR (as shown in Fig. 6) would facilitate the reactions between THz waves and molecules. From the Fig. 7(c), it can be further seen that the reflectivity varies between 0 and 0.62 for g increases from $25 \mu\text{m}$ to $65 \mu\text{m}$. Specifically, the reflectivity reaches a minimum value of $R = 0$ when $g = 45 \mu\text{m}$, i.e., complete coupling between the incident THz radiation and SSPPs wave occurs. So the coupling efficiency between the incident THz wave and SSPPs wave also can be controlled via the coupling gap that cannot be acquired directly by the common direct irradiation modes [13–18], such as the direct excitation of SSPPs modes on grating structure.

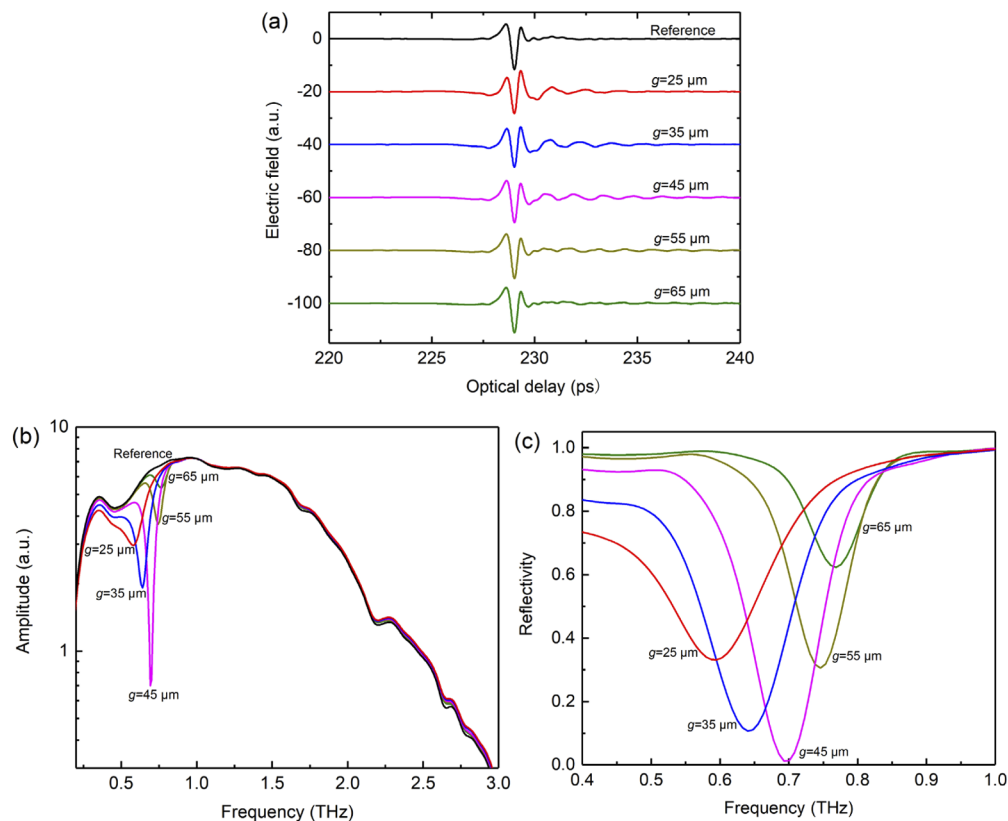


Fig. 7. Experimental time-domain waveforms (a), reflected spectra (b), and reflectivity spectra (c) from the measurement of free-space coupling between THz radiation and SSPPs at different coupling gaps g . The experimental time-domain waveforms are shifted for visual clarity.

Figure 8 shows the experimental time-domain waveforms 8(a), reflected spectra 8(b), and reflectivity spectra 8(c) for two different filling patterns of water (P1 and P2) at their optimum SPR condition (i.e., $R = 0$). The experimental time-domain waveform is also shifted for visual clarity. As it can be seen, both amplitudes of the time-domain waveforms reduced significantly after THz radiation coming out of the HR-Si prism due to the strong absorption of water in THz regime. Nonetheless, there exist two sharp spectral features caused by SPR in the obtained reflected spectra, as shown in Fig. 8(b). Specially, the resonance frequency shifts from 0.695 THz to 0.362 THz for water filled in the grooves (P1), but shifts from 0.695 THz to 0.286 THz for water filled in the gap and grooves (P2), i.e., $\Delta f_1' < \Delta f_2'$, which confirmed the theoretical analysis that analytes filled in the whole resonant cavity can offer a larger sensitivity. Furthermore, the experimental resonance frequencies agree with the theoretical ones reasonably well, as shown in Fig. 4. The slight discrepancy may be caused by the presence of the coupling prism [36] and the fabrication error. By contrast, the filling pattern P2 of material takes full advantage of the enhanced SSPPs electromagnetic field on metasurface surface (as shown in Fig. 6), which maximizes the interaction between light and analytes. Thus, it can support a higher sensitivity. From the Fig. 8(c), it can be seen clearly that these two reflection dips shift and broaden prominently compared with the reflectivity spectrum of air, which further confirm the ultrahigh sensitivity of

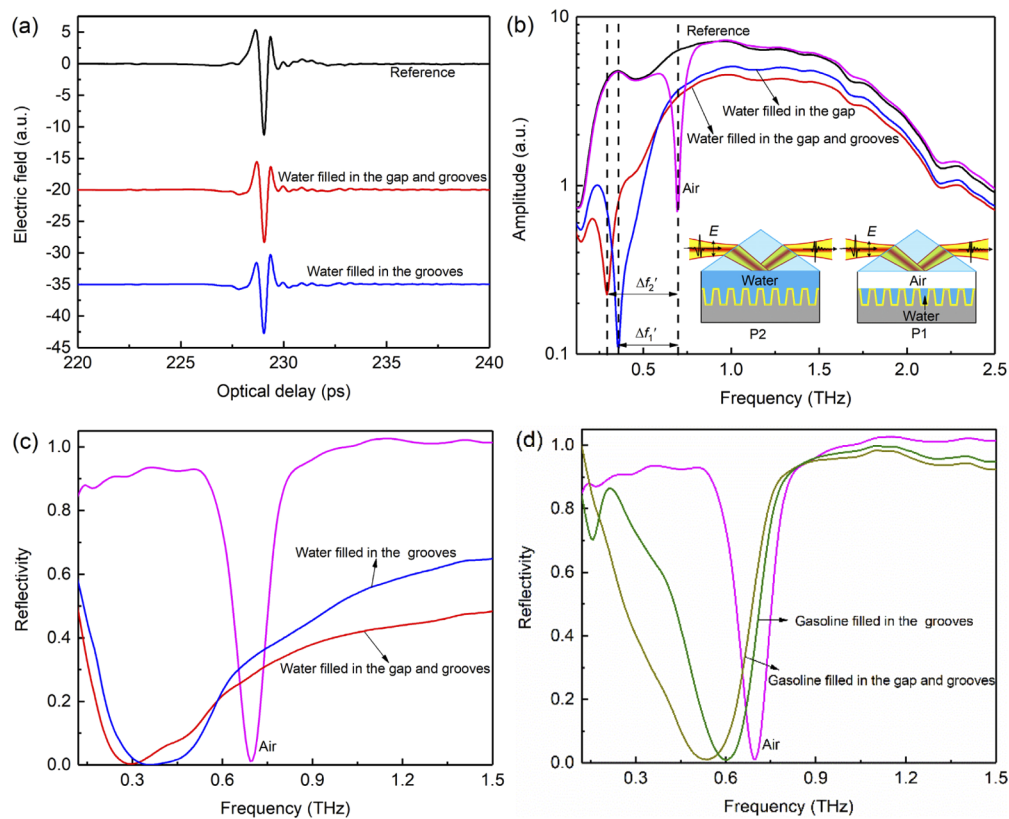


Fig. 8. Experimental time-domain waveforms (a), reflected spectra (b), and reflectivity spectra (c) for two different filling patterns of water: filled in the grooves, and filled in the gap and grooves at their optimum SPR condition. The experimental time-domain waveform is shifted for visual clarity. Experimental reflectivity spectra (d) for two different filling patterns of gasoline: filled in the grooves, and filled in the gap and grooves at their optimum SPR condition.

the SSPPs to the changes in the surrounding dielectric environment. Meanwhile, we also plotted the experimental reflectivity spectra of gasoline ($n = 1.41$, a good spread of refractive index value [21]) for the same filling patterns at their optimum SPR condition, as shown in Fig. 8(d). These two reflection dips shift and broaden obviously as well compared with the reflectivity spectrum of air. Specially, the resonance frequency shifts from 0.695 THz to 0.603 THz for gasoline filled in the grooves (P1), but shifts from 0.695 THz to 0.527 THz for gasoline filled in the gap and grooves (P2), which further prove the superiority of sensing with the filling pattern P2. These experimental results also indicate that this HR-Si prism coupling configuration make it possible for metasurfaces to realize the detection of polar liquids. Compared with conventional direct irradiation methods of SSPPs excitation (such as the direct excitation of SSPPs modes on corrugated metal films [17,18]), this TDS-ATR method is effective to shorten the interaction length of the wave (as shown in the inset of Fig. 2(b)). So the THz radiation attenuation can be minimized when the analytes possess high loss, which is particularly important for THz sensing, especially in biosensing near physiological conditions containing aqueous solutions.

In order to have further insight into the sensitivity for a fixed analyte volume, the variation of simulated resonance frequency versus refractive index of analyte ($n_a = 1, 1.2, 1.4, 1.6, 1.8, \text{ and } 2$) for different analyte quantity (normalized to the volume of groove) and their corresponding linear fitting curves are plotted in Fig. 9(a). The simulated results showed that the resonance frequency has a good linear relation with n_a , which decreases gradually as n_a increases. In particular, the absolute slope of the linear fitting curves (i.e., sensitivity, defined as the change in resonance frequency per RIU) increases gradually as the analyte quantity increases, indicating the increase in analyte quantity will increase the sensitivity. From the Fig. 9(b), it can be further seen that the sensitivity monotonically increases as the analyte quantity increases. Because the enhanced SSPPs electromagnetic field is concentrated mainly at the groove top (as shown in the inset of Fig. 6), so the interaction between analyte and SSPPs wave can be increased as analyte quantity increases. As a result, a higher sensitivity can be obtained.

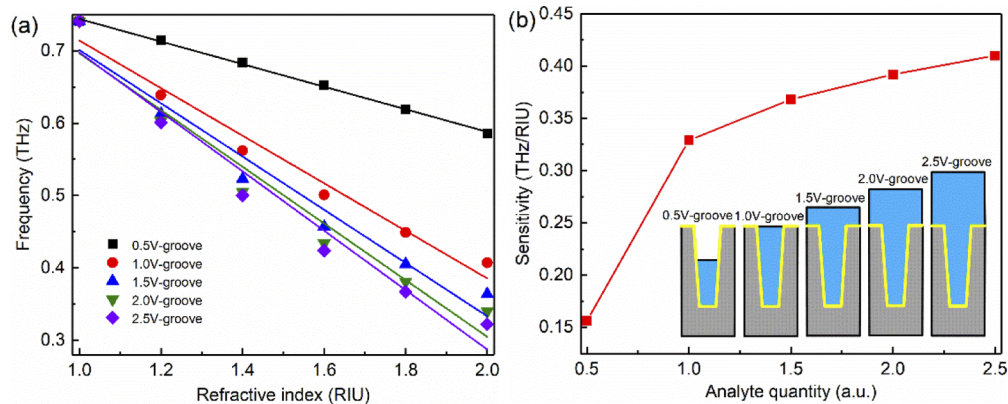


Fig. 9. (a) The variation of simulated resonance frequency versus refractive index of analyte for different analyte quantity (normalized to the volume of groove) and their corresponding linear fitting curves. (b) The variation of sensitivity versus analyte quantity. The insets show the 2D unit cell of the variation of analyte quantity.

4. Conclusions

In conclusion, we have experimentally demonstrated the excitation of the tightly confined SSPPs in THz regime with corrugated metallic metasurface through the HR-Si prism based Otto geometry. In contrast to low refractive index prism, HR-Si prism has shorter the penetration depth of the

evanescent wave, and can achieve larger momentum matching between SSPPs and the evanescent wave. Based on these fantastic properties, HR-Si prism can be utilized as an external coupler to excite more tightly confined SSPPs. Furthermore, the detailed analysis of the dispersion curves reveals that the filling patterns of analyte in the resonant cavity have important effect on the SSPPs resonance mode. Particularly, the interaction between analyte and SSPPs wave can be maximized when the analyte filled with the whole resonant cavity. As a result, an improved sensitivity for THz sensing can be obtained. Apart from THz-SPR sensor, this device might be a very flexible platform for an enhanced detection of molecular THz absorption spectra, which are attributed to the adjustability of the SSPPs by properly controlling the coupling gap. Finally, it is worth noting that the THz radiation attenuation of the existing direct irradiation methods can be alleviated effectively via the HR-Si prism coupling configuration. Compared with the direct excitation of SSPPs modes on grating structure, a higher sensitivity and a complete coupling between the incident THz radiation and SSPPs wave can be achieved by this TDS-ATR method. Although the property of strong absorption in water also leads to an attenuation of the reflected THz radiation, sharp spectral features of water caused by SPR in the obtained reflected spectra, which enables the detection of polar liquids. The THz-SPR technique in combination with ATR method might greatly help the applications of metamaterials in THz-SPR sensing, especially in biosensing near physiological conditions containing aqueous solutions.

Funding

National Natural Science Foundation of China (51675103); Fujian Provincial Department of Science and Technology (2019I0004); State Key Laboratory of Mechanical System and Vibration (MSV-2018-07); Natural Science Foundation of Shanghai (18ZR1414200).

Acknowledgments

Thanks Dr. Gaofeng Zheng of Xiamen University, China for the corrugated metallic metasurfaces processing.

References

1. M. Yin, S. Tang, and M. Tong, "The application of Terahertz spectroscopy to liquid petrochemicals detection: A review," *Appl. Spectrosc. Rev.* **51**(5), 379–396 (2016).
2. S. Zhong, "Progress in terahertz nondestructive testing: A review," *Front. Mech. Eng.* **14**(3), 273–281 (2019).
3. H. Cheon, H. J. Yang, and J. H. Son, "Toward clinical cancer imaging using terahertz spectroscopy," *IEEE J. Sel. Top. Quantum Electron.* **23**(4), 1–9 (2017).
4. K. Siegrist, C. R. Bucher, I. Mandelbaum, A. R. Hight Walker, R. Balu, S. K. Gregurick, and D. F. Plusquellic, "High-resolution terahertz spectroscopy of crystalline trialanine: extreme sensitivity to beta-sheet structure and cocrystallized water," *J. Am. Chem. Soc.* **128**(17), 5764–5775 (2006).
5. J. M. Jornet and I. F. Akyildiz, "Femtosecond-long pulse-based modulation for terahertz band communication in nanonetworks," *IEEE Trans. Commun.* **62**(5), 1742–1754 (2014).
6. J. Liu, J. Dai, S. L. Chin, and X. C. Zhang, "Broadband terahertz wave remote sensing using coherent manipulation of fluorescence from asymmetrically ionized gases," *Nat. Photonics* **4**(9), 627–631 (2010).
7. R. Zhang, Q. Chen, K. Liu, Z. Chen, K. Li, X. Zhang, J. Xu, and E. Pickwell-MacPherson, "Terahertz Microfluidic Metamaterial Biosensor for Sensitive Detection of Small-Volume Liquid Samples," *IEEE Trans. Terahertz Sci. Technol.* **9**(2), 209–214 (2019).
8. J. F. Federici, B. Schulkin, F. Huang, D. Gary, R. Barat, F. Oliveira, and D. Zimdars, "THz imaging and sensing for security applications—explosives, weapons and drugs," *Semicond. Sci. Technol.* **20**(7), S266–S280 (2005).
9. H. Inoue, K. Kawase, Y. Ogawa, and Y. Watanabe, "Non-destructive terahertz imaging of illicit drugs using spectral fingerprints," *Opt. Express* **11**(20), 2549–2554 (2003).
10. M. Walther, P. Plochocka, B. Fischer, H. Helm, and P. U. Jepsen, "Collective vibrational modes in biological molecules investigated by terahertz time-domain spectroscopy," *Biopolymers* **67**(4-5), 310–313 (2002).
11. Y. Huang, S. Zhong, Y. Shen, L. Yao, and D. Cui, "Graphene/Insulator Stack Based Ultrasensitive Terahertz Sensor with Surface Plasmon Resonance," *IEEE Photonics J.* **9**(6), 1–11 (2017).
12. J. Homola, "Surface plasmon resonance sensors for detection of chemical and biological species," *Chem. Rev.* **108**(2), 462–493 (2008).

13. B. Reinhard, K. M. Schmitt, V. Wollrab, J. Neu, R. Beigang, and M. Rahm, "Metamaterial near-field sensor for deep-subwavelength thickness measurements and sensitive refractometry in the terahertz frequency range," *Appl. Phys. Lett.* **100**(22), 221101 (2012).
14. L. Cong, S. Tan, R. Yahiaoui, F. Yan, W. Zhang, and R. Singh, "Experimental demonstration of ultrasensitive sensing with terahertz metamaterial absorbers: a comparison with the metasurfaces," *Appl. Phys. Lett.* **106**(3), 031107 (2015).
15. R. Singh, W. Cao, I. Al-Naib, and L. Cong, "Ultrasensitive terahertz sensing with high-Q fano resonances in metasurfaces," *Appl. Phys. Lett.* **105**(17), 171101 (2014).
16. C. Drexler, T. V. Shishkanova, C. Lange, S. N. Danilov, D. Weiss, S. D. Ganichev, and V. M. Mirsky, "Terahertz split-ring metamaterials as transducers for chemical sensors based on conducting polymers: a feasibility study with sensing of acidic and basic gases using polyaniline chemosensitive layer," *Microchim. Acta* **181**(15-16), 1857–1862 (2014).
17. M. Islam, D. R. Chowdhury, A. Ahmad, and G. Kumar, "Terahertz Plasmonic Waveguide Based Thin Film Sensor," *J. Lightwave Technol.* **35**(23), 5215–5221 (2017).
18. G. Kumar, S. Pandey, A. Cui, and A. Nahata, "Planar plasmonic terahertz waveguides based on periodically corrugated metal films," *New J. Phys.* **13**(3), 033024 (2011).
19. Y. Huang, S. Zhong, Y. Shen, Y. Yu, and D. Cui, "Terahertz phase jumps for ultra-sensitive graphene plasmon sensing," *Nanoscale* **10**(47), 22466–22473 (2018).
20. W. L. Barnes, A. Dereux, and T. W. Ebbesen, "Surface plasmon subwavelength optics," *Nature* **424**(6950), 824–830 (2003).
21. B. Ng, J. Wu, S. M. Hanham, A. I. Fernández-Domínguez, N. Klein, Y. F. Liew, M. B. H. Breese, M. Hong, and S. A. Maier, "Spoof plasmon surfaces: a novel platform for THz sensing," *Adv. Opt. Mater.* **1**(8), 543–548 (2013).
22. X. Hu, G. Xu, L. Wen, H. Wang, Y. Zhao, Y. Zhang, D. R. S. Cumming, and Q. Chen, "Metamaterial absorber integrated microfluidic terahertz sensors," *Laser Photonics Rev.* **10**(6), 962–969 (2016).
23. J. B. Pendry, L. Martínmoreno, and F. J. Garciaavidal, "Mimicking surface plasmons with structured surfaces," *Science* **305**(5685), 847–848 (2004).
24. H. Hirori, K. Yamashita, M. Nagai, and K. Tanaka, "Attenuated total reflection spectroscopy in time domain using terahertz coherent pulses," *Jpn. J. Appl. Phys.* **43**(10A), L1287–L1289 (2004).
25. Y. Zhang, T. Li, B. Zeng, H. Zhang, H. Lv, X. Huang, W. Zhang, and A. K. Azad, "A graphene based tunable terahertz sensor with double fano resonances," *Nanoscale* **7**(29), 12682–12688 (2015).
26. A. K. Azad, J. Dai, and W. Zhang, "Transmission properties of terahertz pulses through subwavelength double split-ring resonators," *Opt. Lett.* **31**(5), 634–636 (2006).
27. A. Otto, "Excitation of nonradiative surface plasma waves in silver by the method of frustrated total reflection," *Z. Phys. A: Hadrons Nucl.* **216**(4), 398–410 (1968).
28. C. R. Williams, S. R. Andrews, S. A. Maier, A. I. Fernández-Domínguez, L. Martín-Moreno, and F. J. García-Vidal, "Highly confined guiding of terahertz surface plasmon polaritons on structured metal surfaces," *Nat. Photonics* **2**(3), 175–179 (2008).
29. C. R. Williams, M. Misra, S. R. Andrews, and S. A. Maier, "Dual band terahertz waveguiding on a planar metal surface patterned with annular holes," *Appl. Phys. Lett.* **96**(1), 011101 (2010).
30. A. P. Hibbins, B. R. Evans, and J. R. Sambles, "Experimental verification of designer surface plasmons," *Science* **308**(5722), 670–672 (2005).
31. H. Yao and S. Zhong, "High-mode spoof spp of periodic metal grooves for ultra-sensitive terahertz sensing," *Opt. Express* **22**(21), 25149–25160 (2014).
32. Y. Huang, S. Zhong, T. Shi, Y. Shen, and D. Cui, "Trapping waves with tunable prism-coupling terahertz metasurfaces absorber," *Opt. Express* **27**(18), 25647–25655 (2019).
33. T. D. Dorney, R. G. Baraniuk, and D. M. Mittleman, "Material parameter estimation with terahertz time-domain spectroscopy," *J. Opt. Soc. Am. A* **18**(7), 1562–1571 (2001).
34. L. Duvillaret, F. Garet, and J. L. Coutaz, "A reliable method for extraction of material parameters in terahertz time-domain spectroscopy," *IEEE J. Sel. Top. Quantum Electron.* **2**(3), 739–746 (1996).
35. A. Rusina, M. Durach, and M. I. Stockman, "Theory of spoof plasmons in real metals," *Appl. Phys. A: Mater. Sci. Process.* **100**(2), 375–378 (2010).
36. C. H. Gan, "Analysis of surface plasmon excitation at terahertz frequencies with highly doped graphene sheets via attenuated total reflection," *Appl. Phys. Lett.* **101**(11), 111609 (2012).